PNAS
RESEARCH ARTICLE | ENGINEERING

Anelasticity in thin-shell nanolattices

I-Te Chen[a,1], Felipe Robles Poblete[b,1], Abhijeet Bagal[b], Yong Zhu[b,2], and Chih-Hao Chang[a,2]

Edited by Yonggang Huang, Northwestern University, Glencoe, IL; received January 28, 2022; accepted August 5, 2022

In this work, we investigate the anelastic deformation behavior of periodic three-dimensional (3D) nanolattices with extremely thin shell thicknesses using nanoindentation. The results show that the nanolattice continues to deform with time under a constant load. In the case of 30-nm-thick aluminum oxide nanolattices, the anelastic deformation accounts for up to 18.1% of the elastic deformation for a constant load of 500 μN. The nanolattices also exhibit up to 15.7% recovery after unloading. Finite element analysis (FEA) coupled with diffusion of point defects is conducted, which is in qualitative agreement with the experimental results. The anelastic behavior can be attributed to the diffusion of point defects in the presence of a stress gradient and is reversible when the deformation is removed. The FEA model quantifies the evolution of the stress gradient and defect concentration and demonstrates the important role of a wavy tube profile in the diffusion of point defects. The reported anelastic deformation behavior can shed light on time-dependent response of nanolattice materials with implication for energy dissipation applications.

anelasticity | 3D nanostructures | nanolattices | nanoindentation

Significance

In this work, the time-dependent deformation and recovery of the nanolattices is measured by a nanoindentation system. The Finite element analysis (FEA) with a defect diffusion model is employed to numerically predict the anelastic behavior of the nanolattices and the results agree reasonably well with the experiments. FEA reveals the role of point defect diffusion induced anelasticity in the time-dependent deformation and recovery in nanolattice structures. The indentation induces bending of the tubular structures, which results in a stress gradient that drives the point defect diffusion within the shells. FEA further shows that the geometric profile of the nanolattices has a dominant influence on the stress gradient and hence the anelastic behavior.

Porous or cellular materials are prevalent in nature and couple both excellent mechanical properties and low density. Such materials including sea sponge skeletons, bones, diatoms, cell walls, and bamboos are widely used for structural support or protection (1–6). However, porous materials with random architecture tend to have poor mechanical properties at low density, therefore ordered architecture that are periodic or hierarchical are important in achieving the maximum strength and stiffness while reducing weight. For example, the skeleton structure of the sea sponges forms a three-dimensional (3D) cylindrical network by orderly arranged cruciform spicules in vertical, horizontal, and diagonal directions along the skin. This intricate and organized architecture significantly increases the strength and stiffness of the structures (5, 7, 8). Additional novel material behavior can be observed when the geometry is scaled down to ∼10 s nm (9–11). Recent works on hallow nanolattices fabricated using two-photon polymerization (TPP) have shown that by decreasing the wall thickness of nanolattices, the material can fully recover even after compression up to 50% (12). Nanolattice films with high optically transparency, low refractive index, low elastic modulus, and strength vs. density scaling as low as 1.1 have also been demonstrated (13–15).

In addition to enhancing strength and stiffness, recent works on engineered nanolattices or nano-architected materials composed of ceramic, metallic, and metallic glass showed large hysteresis/recoverability and associated energy dissipation (10, 12, 16–22). For hollow-tube truss lattices or shell lattices, reducing the thickness of the hollow beams or shells to nanoscale was critical for the recoverability. Shell buckling was proposed to be the precursor of the hysteresis/recoverability. However, the underlying mechanism of how shell buckling leads to the hysteresis/recoverability remains elusive.

Large anelasticity has been reported recently in Al thin film (23) and single nanowires (24, 25). Anelastic solids represent a subset of viscoelastic materials, which manifest in a time-dependent, nonelastic response in addition to an instantaneous elastic response and a full recovery after removal of the load (26). Often termed “internal friction,” anelasticity is typically associated with motion of point defects (27–29), dislocations, grain boundaries, or other types of defects. Anelasticity has been studied in the macroscopic scale but found to be very small (30–33). Recent work has found that single-crystalline ZnO and p-doped Si nanowires under bending can exhibit anelastic behavior that is up to four orders of magnitude larger than the largest anelasticity observed in bulk materials with a recovery time-scale in the order of minutes (22). Experiments and simulations revealed that the large anelasticity is a result of point defect diffusion over nanoscale distances (22, 34–36). While these works advance the knowledge of anelasticity, it is unclear if the large anelasticity observed in single nanowires can occur in 3D sophisticated structures containing nanoscale constituents.

In this work, we demonstrated that anelasticity induced by point defect diffusion is responsible for the hysteresis/recoverability in nanolattice structures. Oxide nanolattices

Author affiliations: [a]Walker Department of Mechanical Engineering, The University of Texas at Austin, Austin, TX 78712; and [b]Department of Mechanical and Aerospace Engineering, North Carolina State University, Raleigh, NC 27695

Author contributions: I.-T.C., F.R.P., Y.Z., and C.-H.C. designed research; I.-T.C., F.R.P., and A.B. performed research; A.B. contributed new reagents/analytic tools; I.-T.C., F.R.P., Y.Z., and C.-H.C. analyzed data; and I.-T.C., F.R.P., Y.Z., and C.-H.C. wrote the paper.

The authors declare no competing interest.

This article is a PNAS Direct Submission.

[1] I.-T.C. and F.R.P. contributed equally to this work.

[2] To whom correspondence may be addressed. Email: yong_zhu@ncsu.edu or chichang@utexas.edu.

This article contains supporting information online at http://www.pnas.org/lookup/suppl/doi:10.1073/pnas.2201589119/-/DCSupplemental.

with thin shell thickness in the range of 30–75 nm were tested with a nanoindenter. After the elastic loading, the nanoindenter was held under a constant load while the displacement increased with time; after the elastic unloading, the displacement decreased with time. This time-dependent deformation and recovery behavior occurred generally for oxide nanolattices with different shell thickness, under different load levels, and for different oxide materials. Finite element analysis (FEA) accounting for the point defect diffusion was able to predict the time-dependent deformation and recovery behavior, in qualitative agreement with the experiments. The coupled mechanical-diffusion model revealed the role of point defect diffusion induced anelasticity in the time-dependent deformation and recovery in nanolattice structures. The indentation induces bending of the thin shells, which results in a stress gradient that drives the point defect diffusion within the shells. In comparison with existing work in 1D nanowires, where anelastic effect is driven by a uniform stress gradient across the diameter under bending, the enabling mechanism in the tubular nanolattice is the wavy profile that give rises to high stress gradients in the hollow shells. This work demonstrates that engineering the geometric profile of nanolattices can be an effective method to control anelastic behaviors.

RESULTS AND DISCUSSION

Nanoindentation Experiment. The deformation behavior of the nanolattice consisting of four stages and the associated anelasticity mechanism is illustrated schematically in Fig. 1. In Stage I, an increasing load is applied to the nanolattice, resulting in elastic bending deformation of the nanolattice. In this stage, the point defect concentration is assumed to remain uniform throughout the structure. The load is then held over a long duration of time to allow the defects to diffuse in the presence of the stress gradient (Stage II). This results in a nonuniform defect concentration profile, which leads to further anelastic deformation of the structure. The load is gradually removed in Stage III, during which the stress gradient induced by the elastic bending deformation is removed. At last, Stage IV is held for an extended amount of time to allow the defects to diffuse back to a uniform concentration profile and enabling the recovery of the anelastic deformation.

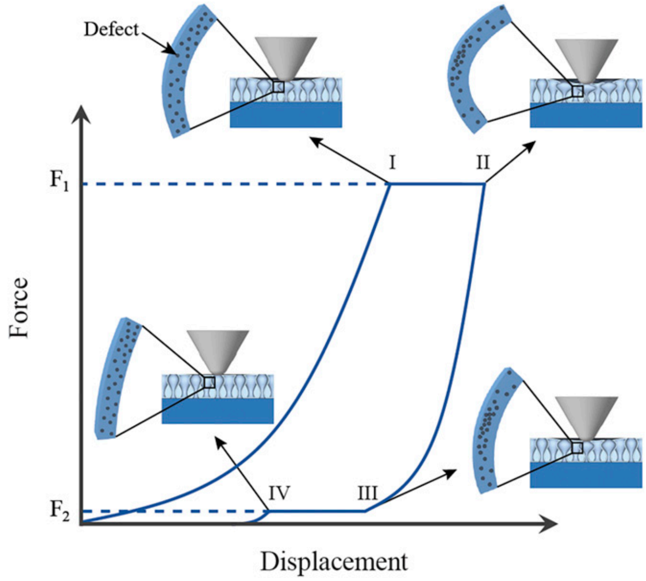

Fig. 1. Schematic of the indentation test. In Stage I, a load with constant loading rate is applied on the nanolattices and results in elastic deformation and stress gradient in the elements. The load is then held constant to allow the diffusion of the defects across the stress gradient, resulting in the anelastic deformation shown in Stage II. In Stage III the load is removed, and the stress gradient induced by the elastic deformation is removed. This stage is held for an extended amount of time to allow the defect to diffuse back to a uniform profile and enabling the recovery of the anelastic deformation in Stage IV.

The 3D periodic nanolattice is fabricated on a silicon substrate using a process that has been previously described (13–15). The fabrication process of the nanolattices is shown in Fig. 2*A*. The periodic photoresist structure is patterned by 3D colloidal lithography using a monodisperse hexagonal-closed-packed nanospheres monolayer (37–40). The periodic features can be controlled by the ratio of the nanospheres diameter and the wavelength of the illumination. The subsequent atomic layer deposition (ALD) process yields a thin conformal coating on the patterned photoresist with a desired thickness. For the anelasticity testing performed in this work, Al_2O_3 and ZnO nanolattices with thickness ranging from 30 nm to 75 nm are deposited in the ALD process. A high-temperature treatment process at 550 °C is employed to remove the sacrificial polymer template, resulting in a thin-shell oxide nanolattice with average radius of 125 nm. The lattice structure in plane is hexagonal-close-packed with a spacing of 500 nm. The details of the fabrication process are provided in the *Materials and Methods* section.

Scanning electron microscope (SEM) images of the nanolattices after removing the photoresist are shown in Fig. 2. Here, it can be observed that the oxide structures are freestanding and periodic. In this work, the nanolattices are one layer, with the thickness of 1 μm. The freestanding Al_2O_3 nanolattices with 30- and 40-nm shell thicknesses are shown in Fig. 2 *B* and *C*, respectively. The Al_2O_3 film is expected to be amorphous for the deposition and annealing conditions (41–44). A ZnO nanolattice with 75 nm in shell thickness, which is polycrystalline (45, 46), as shown in Fig. 2*D*, was fabricated and tested to examine material effects.

The nanoindentation results of the nanolattices are shown in Fig. 3 and a five-data-point simple moving average is employed to mitigate the environmental noise during the measurement. The applied force profile and representative measured displacement vs. time for structures with 30- and 40-nm-thick Al_2O_3 shells are illustrated in Fig. 3*A*. Two force profiles are used, reaching the maximum loads of 500 μN and 800 μN with loading rate of 0.8 and 2.0 mN/min, respectively. Once reaching the maximum load, the indenter holds the constant load for 120 s to examine the anelastic deformation. Here, it can be observed that the nanolattices for both samples continue to deform during the holding period. During unloading, the indenter reduces the load to 10 μN and holds for another 120 s to examine the anelastic recovery. It can be observed that both nanolattices continue to recover during the holding period. Note that the load is reduced to 10 μN rather than zero because a small load (10 μN in this case) must be applied in order to maintain a stable indenter-sample contact. More individual indentation data are included in the *SI Appendix*, section A.

The force-displacement curves in Fig. 3*B* clearly show the time-dependent, anelastic deformation as the forces are held at 500 μN and 800 μN. In the case of 30-nm-thick nanolattices, the indentation displacement increases from 97.5 to 115.1 nm and 130.3 to 149.7 nm under 500 and 800 μN loading, respectively, for 120 s. The similar phenomenon is observed during the unloading process. As the load is held at 10 μN, the displacement keeps decreasing for all the cases. This is the evident of the anelastic recovery as the load is removed. In the case of 30-nm-thick nanolattices (peak load, 500 μN), the indentation displacement reduces from 51.0 nm to 40.9 nm as the load is

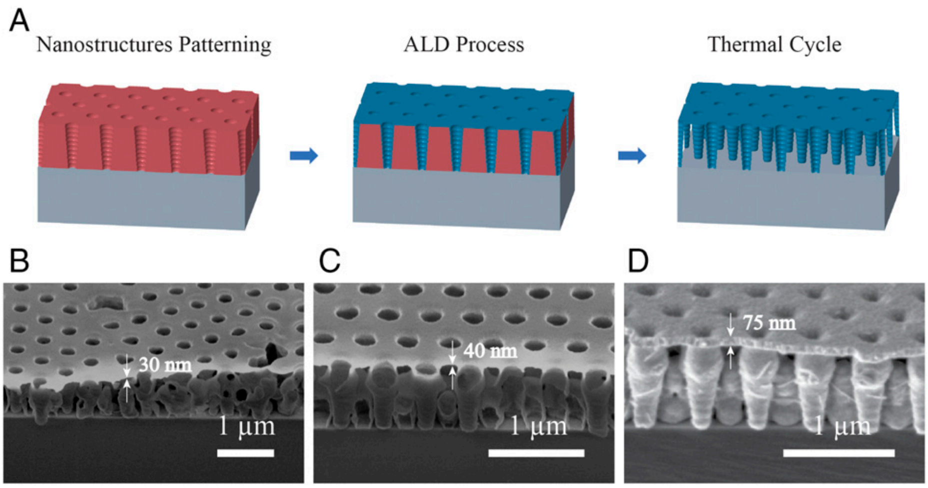

Fig. 2. SEM images of the nanolattice cross-sections. (*A*) Fabrication process of the nanolattices. (*B*) 30 nm Al_2O_3 nanolattices. (*C*) 40 nm Al_2O_3 nanolattices. (*D*) 75 nm ZnO nanolattices.

held at 10 µN for 120 s. For the same 30 nm sample (peak load, 800 µN), the indentation displacement reduces from 85.4 nm to 76.9 nm as the load is held at 10 µN for 120 s.

Two parameters, α_d and α_r, are introduced here to quantify the anelasticity of the nanolattices during the loading and unloading processes, respectively. α_d is defined as the ratio of the anelastic deformation during the holding period (after loading) to the elastic displacement at the maximum load. To illustrate by Fig. 1, α_d is the anelastic deformation in Stage II divided by the maximum displacement at Stage I. Similarly, α_r is defined as the ratio of the anelastic recovery during the holding period (after unloading) to the recovered elastic displacement during unloading. In the Fig. 1, it can be calculated as the anelastic recovery in Stage IV divided by the recovered elastic displacement different in Stage III. The anelastic deformation and recovery ratios over time are shown in Fig. 3 *C* and *D*, respectively. It can be observed in Fig. 3*C* that the anelastic deformation ratio increases rapidly during the first 20 s and then increases more gradually afterward. In the case of 30-nm-thick Al_2O_3 nanolattices, the trends of α_d are similar under different loads. α_d reaches 18.1% and 14.9% under 500 and 800 µN, respectively, after 120 s. The result indicates that the anelastic displacement increases under an increasing load. Similar phenomenon can also be found during the recovery process. As shown in Fig. 3*D*, α_r increases rapidly at first and approaches 15.7% and 9.5% when unloaded from 500 and 800 µN, respectively, after the 120 s hold.

For nanolattices with higher shell thickness, the time-dependent anelastic behavior becomes less evident. As shown in Fig. 3 *B*–*D*, the elastic deformation of a 40-nm thick Al_2O_3 nanolattice under 800 µN loading is 82.3 nm and further reaches 84.3 nm after the 120-s hold time, leading to an anelastic deformation ratio α_r of 2.4%. After reducing the loading to 10 µN, the sample instantly recovers to the indentation depth of 35.6 nm and further reduces 33.7 nm at the end of the 120 s unloading, with the anelastic recover ratio α_d of 3.9%. The 30 nanoindentation test results of the 30-nm nanolattice sample at both 500 and 800 µN hold loads are shown in *SI Appendix*, section A. The time constants of the anelastic deformation and recovery are determined through curve fitting and agree well with the modeled diffusion behavior (*SI Appendix*, Fig. S3).

This anelastic behavior can also be observed in other materials, albeit with different degrees. ZnO nanolattices with 75-nm shell thickness are also examined under 1,000 µN loading, as described in *SI Appendix*, section B. The ZnO nanolattices show 10.1% of α_d and 3.6% of α_r. In addition, the variations of the measurement data are high as well. This can be attributed to the relatively low fabrication yield of the thicker nanolattice samples, which can result in cracks during the thermal treatment process. The anelastic deformation and recovery behavior of ZnO samples with 75-nm shell thickness during the 120 s hold after loading and unloading are shown in the *SI Appendix*, section B.

Finite Element Analysis. To provide mechanistic insights into the observed anelastic behavior, we conducted finite element analysis (FEA) incorporating the diffusion of point defects. The anelasticity in this case is essentially coupled with stress-assisted diffusion. The diffusion equation is given by (47–49)

$$\frac{\partial c}{\partial t} = D\nabla^2 c - D\frac{V}{RT}\nabla c \cdot \nabla\sigma_h - Dc\frac{V}{RT}\nabla^2\sigma_h, \qquad [1]$$

where c is the point defect concentration, D is the diffusivity, $V = 1.4 \times 10^{-29}$ m^3 is the partial molar volume of the point defect (29, 50), R is the universal gas constant, T is the absolute temperature, and σ_h is the hydrostatic stress. In the diffusion model, only one source of point defects, oxygen vacancy, is considered. By solving Eq. **1**, the defect concentration profile for the nanolattice under stress can be calculated as a function of time. Note that here we only consider the stress-driven diffusion, while neglecting the diffusion-induced stresses. The diffusion induced stresses can be estimated by $1/3EVc$ (with E as the Young's modulus) (22, 49), which is orders of magnitude smaller than the bending-induced stresses.

COMSOL Multiphysics was used to solve the 3D coupled structural-diffusion problem, as discussed in more details in *SI Appendix*, section C. The nanolattice structure was modeled as a top plate supported by thin-shell hollow tubes with the wavy and tapered profile as observed in the experiments (Fig. 2). Dimensions of the nanolattice structure were given in accordance with the experimental values. A quarter of the nanolattice structure was modeled in view of the fourfold symmetry of the structure. Two approximations were made in the simulation. First, only four tubes immediately below the indenter tip were simulated (total 16 considering the fourfold symmetry), as shown in Fig. 4*A*, instead of the very large number (>50) of tubes in the experiment. According to our previous work (13), 16 tubes near the contact region can well capture the deformation field, beyond

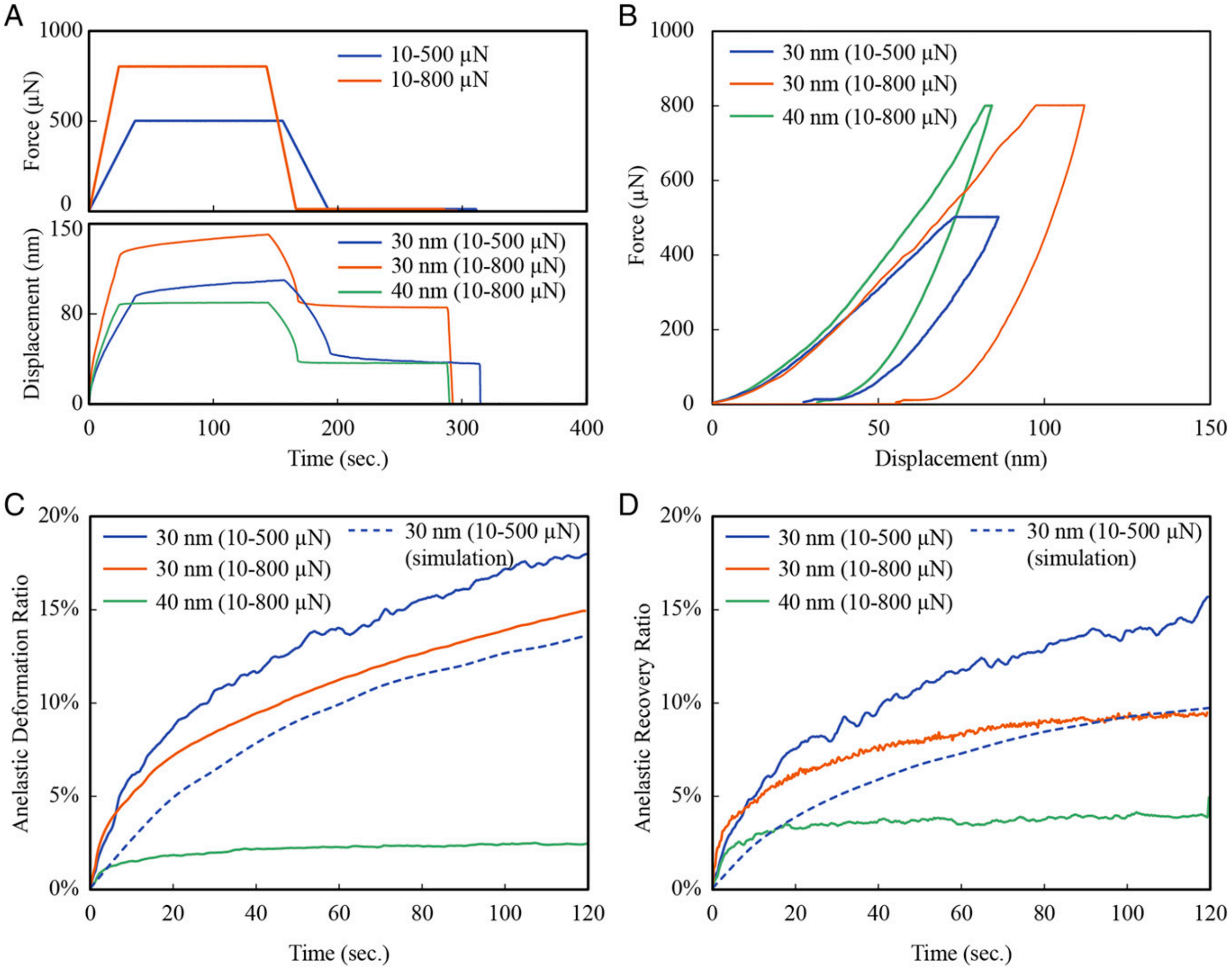

Fig. 3. Nanoindentation results of Al_2O_3 thin-shell nanolattices. (*A*) Force and displacement profiles over time of Al_2O_3 nanolattices. (*B*) Representative force–displacement indentation profiles. (*C*) The anelastic deformation ratio α_d over time during the holding period (after loading). (*D*) The anelastic recovery ratio α_r over time during the holding period (after unloading). In (*C*) and (*D*), the dashed curves are simulation results and all the solid curves are experimental results.

which the deformation is negligible. For the convenience of the subsequent analyses, the x-axis is set to be along the diagonal direction (from the center of the indentation to the corner), as shown in Fig. 4*A*. Second, in COMSOL it is challenging to simulate the full contact mechanics problem in the presence of structural-diffusion coupling. Therefore, we obtained the contact pressure distribution first and then applied the pressure to solve the coupled structural-diffusion problem. Here the pressure distribution was simplified according to the contact between a sphere and a half-space, as given by

$$p(r) = \frac{1}{\pi}\left(\frac{6FE^{*2}}{R^2}\right)^{1/3}\left(1-\frac{r^2}{a^2}\right)^{1/2}, \qquad [2]$$

where F is the applied force, R is the indenter radius, E^* is the reduced modulus defined by $1/E^* = (1-\nu^2)/E + (1-\nu_i^2)/E_i$ with E and ν the Young's modulus and Poisson's ratio of the specimen (Al_2O_3 in this case) and E_i and ν_i the same parameters for the indenter, and $a = \sqrt{Rd}$ is the contact area radius with d the total deformation.

For Al_2O_3, the Young's modulus used was E = 180 GPa while the Poisson's ratio was ν = 0.24. The diffusivity $D = 6.5 \times 10^{-17}$ m^2/s and initial defects concentration $c_{ini} = 4 \times 10^{14}$ m^{-3} were identified by solving the Eq. **1** and comparing the force-displacement curves from experiments and simulations, as shown in Fig. 4*B*. The indentation displacement in the simulation increases from 97.4 to 113.8 nm under 500 μN loading for 120 s and recover from 52.8 to 37.9 nm as the loading reduces from 500 to 10 μN. The corresponding α_d and α_r are 16.8% and 24.5%, respectively. The defects distribution variation during the indentation process is shown in Fig. 4*C*. The simulation result at 0 s means the defects distribution at the moment loading reaches 500 μN. The result of 60 and 120 s show the defects migration during the holding period. The result demonstrates that the defect concentration varies dramatically at the peak and valley of the wavy structures on the tubes.

To further understand the anelastic behavior, the simulated hydrostatic stress, defect diffusion flux, and defect concentration are monitored at three different time stamps during the loading period. The gradient of the hydrostatic stress drives the diffusion of the defects, which can be quantified by the magnitude and direction of the defect flux, as discussed in more details in *SI Appendix*, section D. The defect concentration variation over time at different locations of the tube is shown in Fig. 5, which demonstrates the defect migration behavior. Fig. 5*A* shows the concentration variation along the thickness of the tube at two different locations: the peak (A) and valley (B) of the wavy structure at the center region of the tube. For

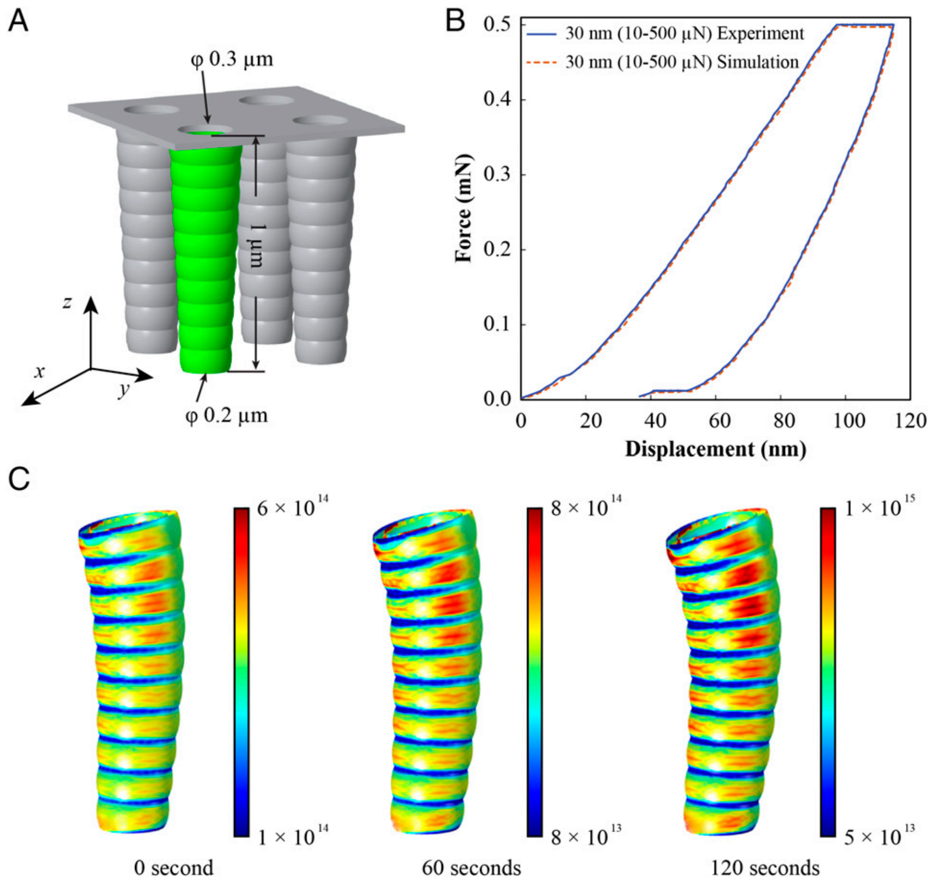

Fig. 4. (*A*) Nanolattice model in COMSOL with the highlighted tube further analyzed. (*B*) Comparison between experiment and simulation in force versus displacement curves during nanoindentation. (*C*) Sequence of images showing tube deformation and defect concentration levels during the holding period from 0 s to 120 s. The unit for the defect concentrations shown is number/m^3.

the wavy geometry, the outer surface at section A sustains a tension while the inner surface is under compression. However, the opposite hydrostatic stress distribution is found on the outer and inner surface at section B. At zero second, the concentration differences across the thickness are 1.41×10^{13} and 9.39×10^{13} m^{-3} at section A and B, respectively. Note that such differences are because the elastic loading (Stage I) took approximately 37 s in accordance with the experiments. However, the hydrostatic gradient across the thickness direction at section A will contribute to the defect diffusion toward the outer edge. The opposite diffusion direction is seen at section B, where the concentration is highest at the inner edge. Thus, the stress gradient will result in more defect migration as time progresses. As a result, the concentration differences through the thickness increase to 5.51×10^{14} and 1.39×10^{15} m^{-3} at section A and B, respectively, after 120 s of the holding period.

The defect concentration varies not only along the shell thickness but also the tube height. Fig. 5*B* shows the concentration along the tube height at the outer edge, illustrating the periodical variation between high and low concentrations at the peak and valley of the wavy structure, respectively. This can be attributed to the high stress gradient from local bending as a result of the wavy profile. The local tension and compression cause the fluctuation of the defect concentration. The defect migration along different hydrostatic gradient can be found by comparing the defect concentration from 0 to 120 s.

Fig. 5 *C* and *D* show the concentrations around the internal and external circumferences at the section A and B, respectively. Here, it can be observed that the postdiffusion concentration is generally higher in the outer edge along section A but in the inner edge along section B, consistent with that shown previously in the through-thickness concentration profile in Fig. 5*A*. Symmetry in the concentration profile along the x-axis (bending direction) is observed in the circumferential direction, however, the variations are relatively small. The maximum and minimum concentrations are along 90 and 270° which corresponding to the diagonal direction of the four-tube module and also the direction of the bending. From the simulated concentration distributions, we can determine that diffusion occurs in all tube directions, namely across the shell thickness and along the tube height between the peak and valley of the wavy profile. There is also diffusion along the circumference, although to a lesser degree.

For the purpose of comparison, the anelastic behavior including the defects and hydrostatic stress distribution of tubes with a tapered but straight profile was studied in the simulation, as discussed in *SI Appendix*, section E. The calculated concentration profile indicates that the dominant diffusion pathway is along the height direction, which has a much lower stress gradient than the wavy tubes. As a result, the anelastic effect is significantly smaller, contributing to anelastic ratios $\alpha_d = 2.1\%$ and $\alpha_r = 3.2\%$, compared with 16.8% and 24.5% for the tubes with the wavy profile. From these results, it is clear that the wavy profile plays a significant role in the observed anelasticity. This effect can be attributed to local bending of the wavy structure, which results in higher stress gradient to drive the diffusion of defects. In the fabrication process used in this work, the wavy tube profiles are result of the interference effects due to the substrate reflection during lithography. The period of the waviness can be calculated as $\lambda/2n$ ($\lambda = 325$ nm, $n \sim 1.6$) or roughly 100 nm for the current samples, which can be seen in the SEM images shown

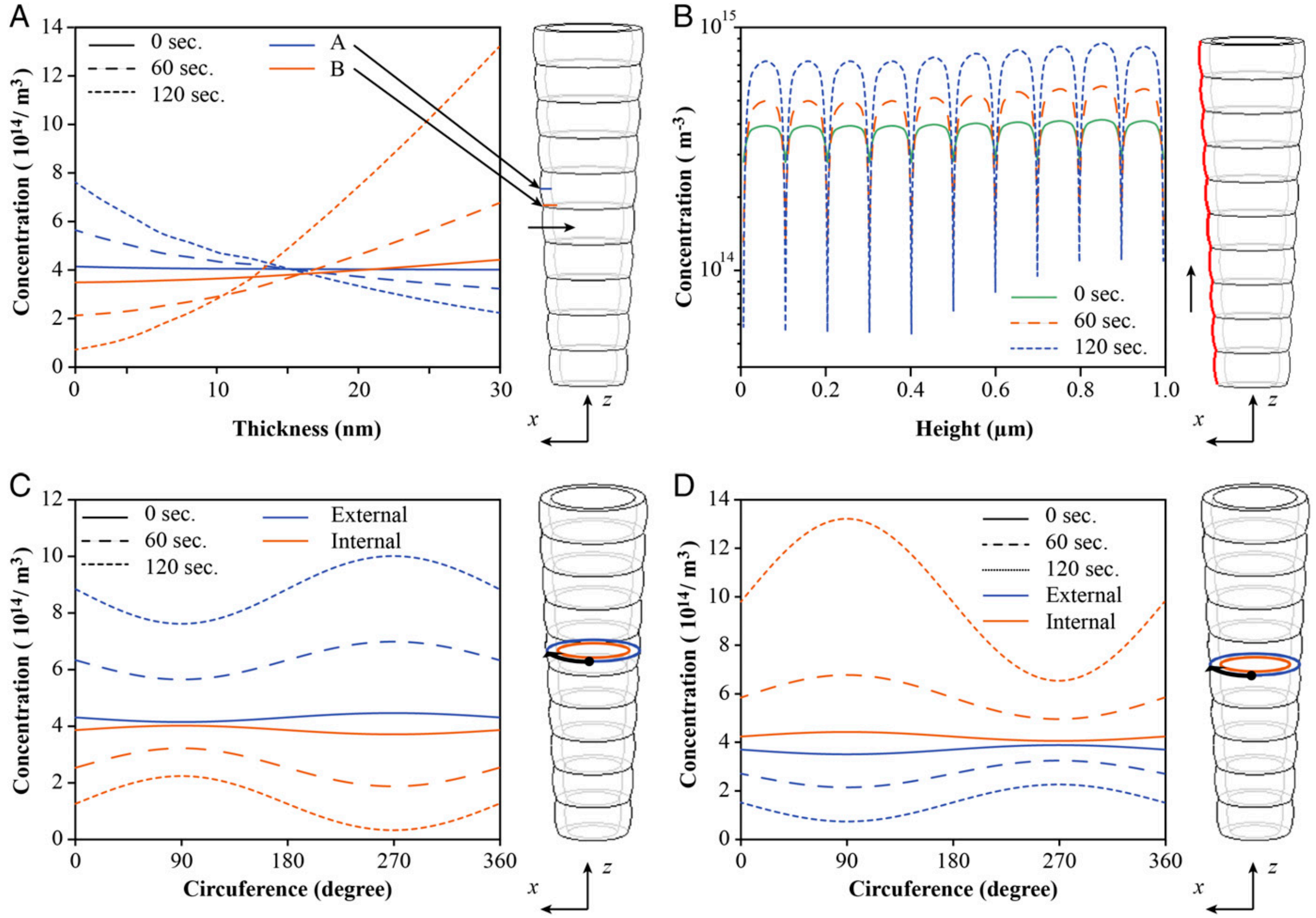

Fig. 5. Defect concentration distribution at different locations. (*A*) Defect concentration distribution across the tube thickness at A and B sections. (*B*) Defect concentration along the height of the tube external shell. (*C*) Defect concentration around the internal and external circumferences of the tube at section A. (*D*) Defect concentration around the internal and external circumferences of the tube at section B.

in Fig. 2. The geometries of the waviness are important factors and can be controlled by the amount of back reflection from the substrate by controlling the thickness of the antireflection coating, which is discussed further in *SI Appendix*, section F. Another effective method to use is TPP, which can more arbitrarily control the structure and wavy profile.

The anelastic effect is expected to have a strong thickness dependency since the through-thickness direction in the tubular element has a high stress gradient and is one of the primary diffusion pathways. The anelastic deformation and recovery ratios as functions of thickness at 120 s have been calculated using the mechanical-diffusion model, as illustrated in *SI Appendix*, Fig. S11 in section G. The results indicate that the anelastic effects decrease significantly to around 5% as the thickness is increased to 50 nm, pointing to the significance of the thin shells. On the other hand, the anelastic effect increases at smaller thickness, as expected. However, in the low thickness limit the highly porous materials have lower stiffness and strength, which can lead to lower overall energy dissipation effects.

While this work investigated the time-dependent response (relaxation and recovery) of a special type of nanolattice, the underlying mechanism of anelasticity could provide valuable insights into the reported recovery in other types of nanolattice structures (11, 12). For example, in the case of hollow 3D ceramic nanolattices fabricated using TPP direct laser writing, large shape recovery was attributed to the elastic shell buckling. In particular, it was reported that localized wrinkling and warping of the tube shells as a result of the shell buckling (12). The wrinkling and warping of the tube shells could resemble the wavy shape and bending in our hollow-tube nanolattice, which can potentially yield anelastic effects.

Another factor to consider is the deformation of the nanolattice in the current work, which consist of a combination of axial compression and bending. The deformation mode examined is significantly more complex than those observed when studying anelasticity in 1D nanowires, which is mostly based on bending alone. The effects of axial loading and bending can be further isolated to study their contributions on the stress gradient in the wavy thin shells. This can be achieved by using nanolattices consisting of stretch-dominated octet-truss and bend-dominated tetrakaidekahedron (Kelvin foam) unit cells, which can be patterned using TPP. However, the wavy profile is still expected to play a significant role for hollow tubular elements in order to induce high stress gradients along the thickness direction.

It is important to know that reported anelastic effect is studied using nanoindentation measurements combined with a coupled mechanical-diffusion model. Our result predicts a high concentration gradient in the thickness direction, which is believed to be one of the dominant defect diffusion pathway. To further validate the constructed model, direct measurement of the concentration as a function of thickness using scanning transmission electron microscopy/electron energy loss spectroscopy (EDS/EELS) during loading would be useful, which has been performed for bending of 1D nanowires (22). However, given the wavy 3D geometry, the small length scale of 500-nm period and tubular elements of the nanolattice, such experiments are difficult to perform without obstruction from neighboring structures.

The observed anelastic behavior in the nanolattices can potentially serve as an energy damping film in microdevices or ultralight energy absorption coating for aerospace, sensor, and biomedical industries. As the nanolattice thin film is flexible and can be uniformly fabricated on a specific area, it can be applied on arbitrary surfaces. The future work will focus on further investigation of the anelastic behavior of nanolattices with different unit cell geometry, tube profile, materials, and thicknesses.

Conclusions

In summary, this work presents the observation and mechanistic understanding of time-dependent anelastic behavior of 3D thin-shelled nanolattices. The deformation is not instantaneous when the indentation force is applied or removed but shows a time-dependent behavior where the lattice continues to deform under a constant load. This phenomenon occurs in a relatively smaller time scale compared with creep and can be attributed to the diffusion of point defects driven by a bending-induced stress gradient. The indentation result of 30 nm Al_2O_3 nanolattices under 500 and 800 μN for 120 s shows 18.1% and 14.9%, respectively, of the anelastic deformation ratio α_d. Upon unloading from 500 and 800 μN, the corresponding anelastic recovery ratio α_r is 15.7% and 9.5%, respectively, after 120 s of holding at 10 μN. The FEA results demonstrate that the wavy structures on the nanolattices play a significant role in the defects diffusion and the anelastic behavior. Due to the higher induced local stress gradients, the nanolattices with the wavy profile have eight times more anelastic ratio than those with the straight profile. The FEA results of the anelastic deformation and recovery ratios are in a qualitative agreement with the experiments. This work sheds light on the anelastic behavior in nanolattice materials, which can find applications for ultra-lightweight energy dissipation.

Materials and Methods

Nanolattice Fabrication. In this work, the silicon substrates (100-mm single-side polished Si wafer, University Wafer) are employed after a layer of antireflection coating (ARC i-con-7, Brewer Science) with approximately 100-nm thickness is applied to avoid the back reflection from the silicon substrates. A photoresist (PFi-88A2, Sumitomo) layer is then spin-coated with the thicknesses of 1 μm. The polystyrene nanospheres with the radius of 500 nm are applied as the periodic phase elements of the near-field lithography. The water–base suspension is first diluted with ethanol and spin-coated on a silicon wafer to achieve a monolayer of nanospheres on the substrate. The coated wafer is then immersed in water and the nanospheres are transferred to the water surface and become hexagonal-closed-packing according to capillary force. Sodium dodecyl sulfate might be used as the surfactant to accelerate the packing process. The monolayer of closed-packing monodispersed nanospheres can be transferred to the photoresist surface as the phase elements. A 325-nm HeCd laser is employed as the light source of the lithography.

Al_2O_3 or ZnO thin films are then coated on the polymer template with ALD process by a custom-made vacuum reactor with viscous-flow, hot-walled ALD system (42, 51, 52). Two self-limiting half reactions are included in ALD process to yield a conformal thin film on the template surface. High purity nitrogen gas (Machin & Welding Supply Co.) which is further purified with an Entegris GateKeeper is employed to purge the reactor after the termination of each self-limiting half reaction. Trimethyl aluminum (TMA, Strem Chemicals, min 98%) is employed as the metal-containing precursor and coreacted with deionized water with the recipe 1/30/1/60 (TMA dose/nitrogen purge/water dose/nitrogen purge in seconds) for Al_2O_3 deposition with the growth rate of 1.1 Å per ALD cycle under the condition of 550 mTorr and 90 °C. Diethyl zinc (DEZ, Strem Chemicals, min 98%) is employed as the precursor to react with deionized water to deposit ZnO under the growth rate of 1.6 Å per DEZ/water ALD cycle. To monitor the film growth and thickness, a silicon wafer (University Wafers, P-type, <1 0 0>) is placed in the front and back of the reactor chamber as the reference sample and further examined by an α-SE ellipsometer (J.A. Woollam Co.) to determine the film thickness.

Nanoindentation Test. A nanoindentation system (Ultra Nano Indentation Tester UNHT, Anton Paar TriTec) is employed in this work for studying the deformation of the nanolattice in nanoscale. The sample is first fixed on the system stage and moved the desired test area under the indenter. A set of indentation tests has 25 test points which are evenly arranged on a 5 × 5 matrix in which each point is 250 μm away in both horizontal and vertical direction from its closest neighborhood. Another three marks are made after the indentation test to locate the position of the test area, and the sample is further inspected with a SEM to check if any pop-in, damages, collapses due to the indentation or the manufacture process happened and exclude the data of these damaged area from the following analysis.

FEA Model. The pillar structure used in the simulation was designed in SolidWorks and exported to COMSOL in the 3D space dimension. Two Physics modules were selected to model the problem: Solid Mechanics (Structural Mechanics toolbox) and General Form PDE (Mathematics toolbox). Only one dependent variable was defined as "c" to account for the point defect concentration in mol/m^3. The Time Dependent study setting was used.

Eq. **1** was input within the general form PDE model in x, y, and z directions in the Conservative Flux section. Both the source term and the mass coefficient were considered to be zero while the damping coefficient was 1. Zero flux was set between the structure and its surrounding. An initial value was chosen for the variable "c." Linear elastic material properties were used in the model. For the model's structural boundary conditions, the bottom of every pillar was fixed while a pressure was applied to the top plate.

Prior to meshing, the structure was partitioned. The time-dependent simulation was set to run in increments of one second and geometry nonlinearity was included in the study. In order to extract the concentration and stress at a particular region, cut lines were defined.

Data Availability. All study data are included in the article and/or *SI Appendix*.

ACKNOWLEDGMENTS. This work was performed in part at the North Carolina State University Nanofabrication Facility and the Analytical Instrumentation Facility, members of the North Carolina Research Triangle Nanotechnology Network, and at the Texas Nanofabrication Facility, which are supported by the National Science Foundation as part of the National Nanotechnology Coordinated Infrastructure (NNCI-2025064 and NNCI-2025227). The authors acknowledge the financial support by the National Science Foundation (CMMI#1552424 and CMMI#1929646).

1. L. J. Gibson, *Cellular Solids: Structure and Properties* (Cambridge University Press, ed. 2, 1997).
2. C. E. Hamm *et al.*, Architecture and material properties of diatom shells provide effective mechanical protection. *Nature* **421**, 841–843 (2003).
3. U. G. K. Wegst, H. Bai, E. Saiz, A. P. Tomsia, R. O. Ritchie, Bioinspired structural materials. *Nat. Mater.* **14**, 23–36 (2015).
4. H. Gao, B. Ji, I. L. Jäger, E. Arzt, P. Fratzl, Materials become insensitive to flaws at nanoscale: Lessons from nature. *Proc. Natl. Acad. Sci. U.S.A.* **100**, 5597–5600 (2003).
5. J. Aizenberg *et al.*, Skeleton of Euplectella sp.: Structural hierarchy from the nanoscale to the macroscale. *Science* **309**, 275–278 (2005).
6. L. R. Meza *et al.*, Reexamining the mechanical property space of three-dimensional lattice architectures. *Acta Mater.* **140**, 424–432 (2017).
7. J. C. Weaver *et al.*, Hierarchical assembly of the siliceous skeletal lattice of the hexactinellid sponge *Euplectella aspergillum*. *J. Struct. Biol.* **158**, 93–106 (2007).
8. M. C. Fernandes, J. Aizenberg, J. C. Weaver, K. Bertoldi, Mechanically robust lattices inspired by deep-sea glass sponges. *Nat. Mater.* **20**, 237–241 (2021).
9. J. Bauer, A. Schroer, R. Schwaiger, O. Kraft, Approaching theoretical strength in glassy carbon nanolattices. *Nat. Mater.* **15**, 438–443 (2016).
10. A. Vyatskikh *et al.*, Additive manufacturing of 3D nano-architected metals. *Nat. Commun.* **9**, 593 (2018).
11. X. Zhang, A. Vyatskikh, H. Gao, J. R. Greer, X. Li, Lightweight, flaw-tolerant, and ultrastrong nanoarchitected carbon. *Proc. Natl. Acad. Sci. U.S.A.* **116**, 6665–6672 (2019).
12. L. R. Meza, S. Das, J. R. Greer, Strong, lightweight, and recoverable three-dimensional ceramic nanolattices. *Science* **345**, 1322–1326 (2014).

13. A. Bagal *et al.*, Large-area nanolattice film with enhanced modulus, hardness, and energy dissipation. *Sci. Rep.* **7**, 9145 (2017).
14. X. A. Zhang *et al.*, Ordered 3D thin-shell nanolattice materials with near-unity refractive indices. *Adv. Funct. Mater.* **25**, 6644–6649 (2015).
15. I.-T. Chen, Z. Dai, Y.-A. Chen, G. N. Parsons, C.-H. Chang, Fabrication of non-uniform nanolattices with spatially varying geometry and material composition. *Adv. Mater. Interfaces.* **8**, 2100690 (2021).
16. L. R. Meza *et al.*, Resilient 3D hierarchical architected metamaterials. *Proc. Natl. Acad. Sci. U.S.A.* **112**, 11502–11507 (2015).
17. T. A. Schaedler *et al.*, Ultralight metallic microlattices. *Science* **334**, 962–965 (2011).
18. A. Torrents, T. A. Schaedler, A. J. Jacobsen, W. B. Carter, L. Valdevit, Characterization of nickel-based microlattice materials with structural hierarchy from the nanometer to the millimeter scale. *Acta Mater.* **60**, 3511–3523 (2012).
19. L. Valdevit, S. W. Godfrey, T. A. Schaedler, A. J. Jacobsen, W. B. Carter, Compressive strength of hollow microlattices: Experimental characterization, modeling, and optimal design. *J. Mater. Res. Warrendale* **28**, 2461–2473 (2013).
20. D. Jang, L. R. Meza, F. Greer, J. R. Greer, Fabrication and deformation of three-dimensional hollow ceramic nanostructures. *Nat. Mater.* **12**, 893–898 (2013).
21. J. Bauer, S. Hengsbach, I. Tesari, R. Schwaiger, O. Kraft, High-strength cellular ceramic composites with 3D microarchitecture. *Proc. Natl. Acad. Sci. U.S.A.* **111**, 2453–2458 (2014).
22. G. Cheng *et al.*, Large anelasticity and associated energy dissipation in single-crystalline nanowires. *Nat. Nanotechnol.* **10**, 687–691 (2015).
23. D. Choi, H. Kim, W. D. Nix, Anelasticity and damping of thin aluminum films on silicon substrates. *J. Microelectromech. Syst.* **13**, 230–237 (2004).
24. Y. Wang *et al.*, Tunable anelasticity in amorphous Si nanowires. *Nano Lett.* **20**, 449–455 (2020).
25. B. Chen *et al.*, Anelastic behavior in GaAs semiconductor nanowires. *Nano Lett.* **13**, 3169–3172 (2013).
26. R. Lakes, *Viscoelastic Materials* (Cambridge University Press, 2009).
27. Ü. Özgür *et al.*, A comprehensive review of ZnO materials and devices. *J. Appl. Phys.* **98**, 041301 (2005).
28. L. Schmidt-Mende, J. L. MacManus-Driscoll, ZnO – Nanostructures, defects, and devices. *Mater. Today* **10**, 40–48 (2007).
29. A. Janotti, C. G. Van de Walle, Native point defects in ZnO. *Phys. Rev. B Condens. Matter Mater. Phys.* **76**, 165202 (2007).
30. G. Schaumann, J. Völki, G. Alefeld, The diffusion coefficients of hydrogen and deuterium in vanadium, niobium, and tantalum by gorsky-effect measurements. *Phys. Status Solidi, B Basic Res.* **42**, 401–413 (1970).
31. G. Schaumann, J. Völkl, G. Alefeld, Relaxation process due to long-range diffusion of hydrogen and deuterium in niobium. *Phys. Rev. Lett.* **21**, 891–893 (1968).
32. C. Zener, C. S. Smith, C. S. Barrett, E. A. Long, *Elasticity and Anelasticity of Metals* (University of Chicago Press, ed. 1, 1948).
33. A. S. Nowick, B. S. Berry, Anelastic Relaxation in Crystalline Solids (Academic, 1972).
34. T. Zhu, J. Li, Ultra-strength materials. *Prog. Mater. Sci.* **55**, 710–757 (2010).
35. D. S. Gianola, J. Shin, Nanomechanics: Full recovery takes time. *Nat. Nanotechnol.* **10**, 659–660 (2015).
36. S. Wang, Z. Shan, H. Huang, The mechanical properties of nanowires. *Adv. Sci. (Weinh.)* **4**, 1600332 (2017).
37. C.-H. Chang *et al.*, From two-dimensional colloidal self-assembly to three-dimensional nanolithography. *Nano Lett.* **11**, 2533–2537 (2011).
38. J.-H. Min, X. A. Zhang, C.-H. Chang, Designing unit cell in three-dimensional periodic nanostructures using colloidal lithography. *Opt. Express* **24**, A276–A284 (2016).
39. X. A. Zhang, I.-T. Chen, C.-H. Chang, Recent progress in near-field nanolithography using light interactions with colloidal particles: From nanospheres to three-dimensional nanostructures. *Nanotechnology* **30**, 352002 (2019).
40. I.-T. Chen, E. Schappell, X. Zhang, C.-H. Chang, Continuous roll-to-roll patterning of three-dimensional periodic nanostructures. *Microsyst. Nanoeng.* **6**, 22 (2020).
41. D. M. Hausmann, R. G. Gordon, Surface morphology and crystallinity control in the atomic layer deposition (ALD) of hafnium and zirconium oxide thin films. *J. Cryst. Growth* **249**, 251–261 (2003).
42. B. Gong *et al.*, Sequential vapor infiltration of metal oxides into sacrificial polyester fibers: Shape replication and controlled porosity of microporous/mesoporous oxide monoliths. *Chem. Mater.* **23**, 3476–3485 (2011).
43. J. W. Elam, C. A. Wilson, M. Schuisky, Z. A. Sechrist, S. M. George, Improved nucleation of TiN atomic layer deposition films on SiLK low-k polymer dielectric using an Al2O3 atomic layer deposition adhesion layer. *J. Vac. Sci. Technol. B Microelectron. Nanometer Struct. Process. Meas. Phenom.* **21**, 1099 (2003).
44. J. D. Ferguson, A. W. Weimer, S. M. George, Atomic layer deposition of Al2O3 films on polyethylene particles. *Chem. Mater.* **16**, 5602–5609 (2004).
45. T. Tynell, M. Karppinen, Atomic layer deposition of ZnO: A review. *Semicond. Sci. Technol.* **29**, 043001 (2014).
46. J. W. Elam, S. M. George, Growth of ZnO/Al2O3 alloy films using atomic layer deposition techniques. *Chem. Mater.* **15**, 1020–1028 (2003).
47. S. Serebrinsky, E. A. Carter, M. Ortiz, A quantum-mechanically informed continuum model of hydrogen embrittlement. *J. Mech. Phys. Solids* **52**, 2403–2430 (2004).
48. F. Yang, Interaction between diffusion and chemical stresses. *Mater. Sci. Eng. A* **409**, 153–159 (2005).
49. H. Haftbaradaran, J. Song, W. A. Curtin, H. Gao, Continuum and atomistic models of strongly coupled diffusion, stress, and solute concentration. *J. Power Sources* **196**, 361–370 (2011).
50. P. Erhart, K. Albe, A. Klein, First-principles study of intrinsic point defects in ZnO: Role of band structure, volume relaxation, and finite-size effects. *Phys. Rev. B Condens. Matter Mater. Phys.* **73**, 205203 (2006).
51. J. C. Spagnola *et al.*, Surface and sub-surface reactions during low temperature aluminium oxide atomic layer deposition on fiber-forming polymers. *J. Mater. Chem.* **20**, 4213 (2010).
52. J. S. Jur *et al.*, Temperature-dependent subsurface growth during atomic layer deposition on polypropylene and cellulose fibers. *Langmuir* **26**, 8239–8244 (2010).